Supporting Information

Renz et al. 10.1073/pnas.1211753109

SI Experimental Procedures

Mammalian Plasmids. Rat asialoglycoprotein receptor subunits, rat hepatic lectin 1 (RHL1) and RHL2 (NM_012503 and NM_017189), were amplified as *XhoI-SacII* fragments using the N-terminal primers 5′-AAA TTC TCG AGC ATG ACA AAG GAT TAT CAA GA-3′ for RHL1 and 5′-AAA TTC TCG AGT ATG GAG AAG GAC TTT CAA G-3′ for RHL2 containing an *XhoI* site (underlined) and the C-terminal primers 5′-ATA ATC CGC GGC TAA TTG GCC TTG CCC AAC-3′ for RHL1 and 5′-ATA ATC CGC GGC TAG TAG GTG ATG TCC CGT TTC C-3′ for RHL2 containing an *SacII* site (underlined), and inserted into a Clontech C2 vector. RHL1Δ (RHL1Δ68–119) was constructed using *BglII* and *XbaI* restriction, Klenow polymerase, and site-directed mutagenesis to correct for frame shift (primers 5′-CCC AAC TCC GGG AAT CTA GAT TGC TAC TGC-3′ and 5′-GCA GTA GCA ATC TAG ATT CCC GGA GTT GGG-3′). RHL1Δc (RHL1Δ68–143) was generated using site-directed mutagenesis and the primers 5′-CAA AAT TCC CAA CTC CGG GAA CGG GGC AAT GGC TCT GAA AGG-3′ and 5′-CCT TTC AGA GCC ATT GCC CCG TTC CCG GAG TTG GGA ATT TTG-3′. RHL1TM (RHL1Δ66–284) and RHL2TM (RHL2Δ85–301) were constructed using the C-terminal primers 5′-ATA ATC CGC GGT CAG AGT TGG GAA TTT TGG-3′ and 5′-ATA ATC CGC GGT CAC AGC TGC ATG CTT TG-3′ containing an *SacII* restriction site (underlined). eGFP, mCherry1, PA-mGFP (1), and PA-mCherry1 (2) were inserted using the restriction sites *AgeI* and *BsrGI*. Fig. S2 provides an overview of WT and mutant RHL used in this study.

To construct two- and three-color fusion probes, PA-mGFP, PA-mCherry1, and mCherry1 were inserted into a Clontech N1 vector using the restriction sites *AgeI* and *BsrGI*. PA-mGFP and mGFP were amplified as an *SalI–BamHI* fragment using the N-terminal primer 5′-AAT TAA CAG TCG ACG ATG GTG AGC AAG GGC GAG G-3′ containing an *SalI* site (underlined) and the C-terminal primer 5′-AAT ATA TGG ATC CCG CTT GTA CAG CTC GTC CAT GC-3′ containing a *BamHI* site (underlined) inserted into the multiple cloning site of the N1 vector. mGFP-mCherry1 and PA-mGFP-PA-mCherry1 fusion constructs were generated. PCR-amplified *EcoRI-SalI* fragments of PA-mGFP and PA-mCherry1 using the N-terminal primer 5′-AA ATT AGA ATT CTG GGT ATG GTG AGC AAG GGC GAG G-3′ containing an *EcoRI* site (underlined) and the C-terminal primer 5′-ATA ATT GTC GAC TGC TTG TAC AGC TCG TCC ATG C-3′ containing an *SalI* site (underlined) were additionally inserted to generate a triple-color fusion construct. The vesicular stomatitis virus glycoprotein (VSVG) was inserted from the VSVG-mGFP N1 plasmid using the restriction enzymes *BglII* and *EcoRI* to generate VSVG-PAmGFP-PAmCherry1, VSVG-PAmGFP-PAmGFP-PAmCherry1, and VSVG-PAmCherry1-PAmGFP-PAmCherry1, respectively. For simplicity, we refer to the fluorescent proteins used as GFP, Cherry, PA-GFP, and PA-Cherry.

Cell Culture. Normal rat kidney (NRK) and COS-7 cells (CV-1 Origin SV40 cells) were cultured in DMEM without phenol red and supplemented with 10% FBS, 100 mM sodium pyruvate, and 2 mM glutamine (Invitrogen). Cells were grown in eight-well LabTek chambers with #1.0 cover glass for confocal microscopy and 18-mm #1.5 cover glass (Warner Instruments) for photo-activated localization microscopy (PALM) analyses. They were transfected 24 h after plating with Fugene6 (Roche); 20 h

posttransfection, cells were fixed in 4% paraformaldehyde (Electron Microscopy Sciences) for 15 min at room temperature and washed two times with 50 mM glycine, two times with 50 mM glycine plus 1 mg/mL sodium borate in PBS, and finally, three times with PBS.

Labeling of Asialofetuin and Lactoferrin. Asialofetuin (A-4781; Sigma) was labeled with amine-reactive Alexa647 (A-20006; Invitrogen) according to the manufacturer's protocol. Lactoferrin (L-4765; Sigma) was labeled with thiol-reactive Alexa647 (A-20347; Invitrogen) according to the manufacturer's protocol. An average labeling degree of about 2 mol dye per 1 mol protein was achieved. Cells were incubated at 4 °C for 45 min in DMEM with excess Alexa647-tagged asialofetuin or lactoferrin, respectively. They were washed and then incubated with prewarmed medium at 37 °C for ligand uptake.

Confocal Microscopy. Cell imaging was performed on a Zeiss LSM510 confocal laser scanning microscope equipped with a 63× Plan Apochromat N.A. 1.4 oil immersion objective. The 488-nm line of an argon ion laser (Lasos) and 543- and 633-nm HeNe diode lasers (Lasos) were used to excite GFP, Cherry, and Alexa-647, respectively. Dichroic mirrors on LSM510 were 488/543 and 488/543/633. Fluorescence from GFP was collected through a 505- to 530-nm band pass. Fluorescence from Cherry and PA-Cherry was collected with a 585-nm long pass or a 585- to 615-nm band-pass filter, and fluorescence from Alexa-647 was collected with a 650-nm long-pass filter.

Determination of Pixel-by-Pixel FRET Efficiencies in a Confocal Image. FRET measurements were performed on the Zeiss LSM 510 confocal laser scanning microscope as previously described (3). Donor signal I_1 (excitation = 488 nm, emission = 505–530 nm), FRET signal I_2 (excitation = 488 nm, emission > 585 nm), and acceptor signal I_3 (excitation = 543 nm, emission > 585 nm) were collected. These fluorescence intensities have contributions from direct excitation of donor and acceptor, sensitized emission of the acceptor, and cellular autofluorescence, and they can be expressed as follows (Eq. **S1**):

$$I_1(488, 505 - 530) = I_D(1 - E) + B_1, \tag{S1}$$

(Eq. **S2**)

$$I_2(488, > 585) = I_D(1 - E)S_1 + I_A S_2 + I_D E\alpha + B_2, \text{ and} \tag{S2}$$

(Eq. **S3**)

$$I_3(543, > 585) = I_A + B_3, \tag{S3}$$

where I_D is the unquenched donor signal in channel 1 that would be measured in the absence of acceptor, I_A is the acceptor signal in channel 3, and E is the mean FRET efficiency. Average background intensities in the respective channels B_1, B_2, and B_3 were determined from nontransfected cells. Spectral cross-talk factors, S_1 and S_2, were calculated using cells expressing only GFP or Cherry, respectively (Eq. **S4**):

$$S_1 = \frac{I_2 - B_2}{I_1 - B_1} \quad \text{and} \tag{S4}$$

(Eq. **S5**)

$$S_2 = \frac{I_2 - B_2}{I_3 - B_3}. \quad \text{[S5]}$$

The factor α relates the signal from any given number of excited GFP molecules in channel 1 to the signal from an equal number of excited Cherry molecules in channel 2. It is defined by (Eq. **S6**)

$$\alpha = \frac{Q_A \eta_A}{Q_D \eta_D}, \quad \text{[S6]}$$

where Q_D and Q_A are the fluorescence quantum yields of GFP and Cherry and η_D and η_A are the detection efficiencies (including emission filter transmissions, detector sensitivities, and amplifications) of donor and acceptor fluorescence in channels 1 and 2, respectively. Technically, α can be determined from two samples expressing known amounts of GFP and Cherry using Eq. **S7**:

$$\alpha = \frac{I_2^A \varepsilon^D(488) N^D}{I_1^D \varepsilon^A(488) N^A}, \quad \text{[S7]}$$

where I_2^A is the directly excited fluorescence of the acceptor, I_1^D is the fluorescence of the donor, $\varepsilon^D(488)$ and $\varepsilon^A(488)$ are the extinction coefficients of donor and acceptor at 488 nm, and N^D/N^A is the ratio of donor and acceptor molecules expressed by the sample. Knowing S_1, S_2, and α, Eq. **S1** can be solved for E, I_D, and I_A for each cell (Eq. **S8**):

$$E = 1 - \frac{1}{1 + \frac{1}{\alpha}\left(\frac{(I_2 - B_2) - S_2(I_3 - B_3)}{I_1 - B_1} - S_1\right)}. \quad \text{[S8]}$$

Because it is not straightforward to determine the ratio of GFP and Cherry molecules expressed in distinct cell populations, the calculation of α poses a problem. We assessed α by using cells expressing a GFP-Cherry fusion protein, in which the N^D/N^A ratio is one. Because of FRET between donor and acceptor molecules, the unquenched I_D donor intensity and the directly excited acceptor fluorescence I_A cannot be determined directly. Therefore, a successive approximation was used for determining α and E simultaneously (3) (Eq. **S9**):

$$\alpha = \frac{(I_3 - B_3) \times S_2 \times (1 - E)}{I_1 - B_1} \times \frac{\varepsilon^D(488)}{\varepsilon^A(488)}. \quad \text{[S9]}$$

Using the GFP-Cherry fusion protein, the FRET-corrected acceptor-to-donor intensity ratio Q was calculated (Eq. **S10**):

$$Q = \frac{(I_3 - B_3) \times (1 - E)}{I_1 - B_1}. \quad \text{[S10]}$$

For other cotransfected cells, the molecular acceptor-to-donor ratio N^A/N^D was assessed as (Eq. **S11**)

$$N^A/N^D = \frac{(I_3 - B_3) \times (1 - E)}{(I_1 - B_1) \times Q}. \quad \text{[S11]}$$

To minimize spectral spillover, alternating laser excitation was used. Images were low pass-filtered and further processed in a customized ImageJ routine to assess FRET efficiency E and acceptor-to-donor ratio on a pixel-by-pixel basis. Images were background-subtracted, and only pixels above the threshold (2.5 × background) were further analyzed. Mean cellular FRET efficiencies were normalized to the FRET efficiency of the positive control—the

GFP-Cherry fusion protein (the absolute FRET efficiency for this protein was $E = 0.3$, which corresponds to 100% on the normalized FRET efficiency scale). Results were false-colored and displayed as images of pixel-by-pixel FRET efficiency maps. For analyzing asialoglycoprotein receptor homo- and hetero-oligomerization, only pixels constituting the plasma membrane at the rim of cells were delineated and considered, and internal pools were disregarded.

Mathematical Modeling. We developed a model to test analytically the schematic explanation of the experimental data for RHL1/RHL2 hetero-oligomerization shown in Fig. 3C. To model FRET efficiency, E, as determined by the fraction of donor, D, that is part of a complex and can, therefore, be quenched, we considered a reaction equilibrium described by the law of mass action. We begin with the mass action binding expression (**S12**),
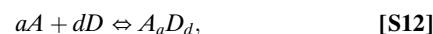
$$aA + dD \Leftrightarrow A_a D_d, \quad \text{[S12]}$$

where A is the acceptor, D is the donor, and a and d are the respective integer stoichiometries. The equilibrium constant is given by (Eq. **S13**)

$$K = \frac{[A_a D_d]}{[A]^a [D]^d}. \quad \text{[S13]}$$

The total amounts of each species [i.e., total amount of acceptor A (T_A) and donor D (T_D)] are given by (Eq. **S14**)

$$T_A = [A] + a[A_a D_d]. \quad \text{[S14]}$$

Therefore (Eq. **S15**),

$$[A] = T_A - a[A_a D_d], \quad \text{[S15]}$$

and for the donor, D (Eq. **S16**),

$$T_D = [D] + d[A_a D_d]. \quad \text{[S16]}$$

Therefore (Eq. **S17**),

$$[D] = T_D - d[A_a D_d]. \quad \text{[S17]}$$

Thus, inserting Eqs. **S15** and **S17** into Eq. **S13** results in (Eq. **S18**)

$$K = \frac{[A_a D_d]}{(T_A - a[A_a D_d])^a (T_D - d[A_a D_d])^d} \quad \text{[S18]}$$

or (Eq. **S19**)

$$K \star (T_A - a[A_a D_d])^a (T_D - d[A_a D_d])^d = [A_a D_d] \quad \text{[S19]}$$

or (Eq. **S20**)

$$K \star (T_A - aC)^a (T_D - dC)^d = C. \quad \text{[S20]}$$

Thus (Eq. **S21**),

$$K \star (T_A - aC)^a (T_D - dC)^d - C = 0, \quad \text{[S21]}$$

where $C = [A_a D_d]$ or complex.

The order of the equation depends on the order of the reaction (i.e., the integer value of a and d). We then analytically

solved the resulting quadratic, cubic, or quartic equation to obtain (Eq. **S22**)

$$E \propto \frac{d[A_a D_d]}{T_D} = \frac{d[C]}{T_D} \qquad \textbf{[S22]}$$

as a function of acceptor-to-donor ratio, $\frac{T_A}{T_D}$.

We assumed quenching of free donor to be negligible. The relative contributions to overall FRET efficiencies of different homocomplexes were tuned with free parameter leading coefficients.

Applying integer stoichiometries of $a = 1$ and $d = 2$ (i.e., one acceptor on two donors in a complex) or $a = 2$ and $d = 1$ (i.e., two acceptors on one donor in a complex) yielded the curves shown in Fig. 3D. These curves fit the experimental data of RHL1 and RHL2 hetero-oligomerization.

PALM. Glass slides were washed by boiling in acetone for 10 min at 75 °C and then, a mixture of 1:1:5 $H_2O_2/NH_4OH/H_2O$ for 90 min at 75 °C; finally, they were thoroughly rinsed in Milli-Q filtered water (Millipore). To dedrift and overlay two-color images, TetraSpecks (Invitrogen) were used as fiducial markers. TetraSpecks were sonicated, diluted 1:1,300 in Milli-Q filtered water, and dried on coverslips before cell plating.

PALM imaging was performed on an Olympus IX81 microscope using a 60× 1.45 N.A. Plan Apo N total internal reflection fluorescence (TIRF) objective (Olympus) as previously described (4). The following lasers were used: a 40-mW, 561-nm Compass, a 50-mW, 488-nm Sapphire, and a 50-mW, 405-nm Cube (Coherent). To prevent photon loss and spherical aberrations that occur during simultaneous imaging with devices such as the DualView system (Photometrics), the following protocol of low-light illumination for sequential measurements was developed (Fig. S8). First, 488-nm light alone is used to activate and excite PA-GFP; 488-nm light is set to a low power density of 30 W/cm² (250 µW as measured at the rear pupil, and illumination spot size of 25 µm in diameter). To not lose PA-GFP molecules at the beginning of any data acquisition, acquisition was started while searching for transfected cells (Movie S1). When no additional PA-GFPs are registered, illumination is switched to 405 nm to activate and 561 nm to excite PA-Cherry; 561-nm light is set to a low power density of 40 W/cm² (400 µW as measured at the rear pupil, and illumination spot size of 30 µm in diameter). Power density of the 405-nm laser is initially set to 0.01 W/cm² and then gradually increased to 3 W/cm², minimizing photobleaching and oversampling of PA-Cherry molecules during the early periods of collection. After PA-Cherry is exhausted, 488-nm illumination is again applied, and 405-nm activation is set to high power density (3 up to 500 W/cm²); 405-nm light is used to measure PA-GFP molecules, which might not have been accessible by 488-nm activation alone.

Excitation (488 and 561 nm) was alternated with 405 nm to reduce bleed-through of the 405-nm light. Fluorescence was detected with an Andor iXon EM-CCD DV 887ECS-BV (Andor Technology). Exposure time was set to 100 ms, with a readout pause of 106 ms. The resulting frame rate was 5 frames/s.

Single-Molecule Counting PALM Analysis. Intensity peaks were localized using a previously described algorithm written in IDL (Research Systems, Inc.) (5). In PALM, a single fluorophore may emit photons over multiple consecutive frames before being photobleached. This finding is especially true under conditions of low-light illumination because of less photobleaching. Therefore, it is essential to assign properly single molecular events. We used the peak distributions of single molecules (Figs. S10B and S11) as the basis for adapting the grouping parameters. Grouping parameters define spatial and temporal limits within which isolated peaks are assumed to originate from one molecule. Although the spatial limit is based on the fit precision, the temporal limit considers how long a fluorescent protein can blink off. Blinking characteristics of fluorescent proteins in the long time range are poorly characterized. GFP off-times may last up to several seconds (6). Isolated peaks of PA-GFP and PA-Cherry were grouped, and a blinking time of 4 s and a grouping radius of 67 nm were applied, which equals three times the uncertainty of the 2D Gaussian fit and covers 99.5% of possible fitted positions (Figs. S9 and S10).

Signal-to-noise ratio (SNR) was calculated as the difference in mean intensity between object (I_o) and background (I_b) divided by noise of object (σ_o) and background (σ_b) (7) (Eq. **S23**):

$$SNR = (I_a - I_b)/\sqrt{\sigma_a^2 + \sigma_b^2}. \qquad \textbf{[S23]}$$

Additional data analysis was performed in Kaleidagraph (Synergy Software). Plotting a larger y range against frame number reveals a population of insufficiently fixed, still mobile molecules (Fig. S12). Those molecules cover a large distance (up to 1 µm) in a short time (Fig. S12C and Movie S3). To reduce the number of moving molecules, groups containing one event were subtracted. Applying the imaging protocol and peak assignment regimen described, cells expressing the VSVG-PA-GFP-PA-Cherry were measured. Given a 1:1 expression of PA-Cherry and PA-GFP, the relative detection efficiency of the experimental setup can be assessed. Red single-molecule counts were plotted vs. green single-molecule counts of each cell. Using least squares, data were fit to a linear function with an intercept of zero. Its slope of 1.1 provides the setup-specific relative detection efficiency. For assessment of stoichiometries, the number-based red-to-green ratio of each cell expressing the VSVG-PA-Cherry-PA-GFP-PA-Cherry and VSVG-PA-GFP-PA-GFP-PA-Cherry was normalized to this relative detection efficiency of 1.1.

The relative expression of PA-GFP-RHL1 and PA-Cherry-RHL1 or PA-GFP-RHL1 and PA-Cherry-RHL2 was determined using the same experimental and analytical approach. To determine the numerical proportion in a larger membrane area, the number-based red-to-green ratio of each cell was normalized to the relative detection efficiency of 1.1. To assess the stoichiometry of molecules in a cluster, clusters were defined using a nearest neighbor algorithm written in Matlab (Mathworks; http://www.mathworks.com/matlabcentral/fileexchange/12574-nearestneighbour-m). For each molecule, neighbors within a user-defined radius (here, 100 nm) were determined by Euclidian distance. Only clusters comprising at least 10 molecules were further analyzed. Red single-molecule counts were plotted vs. green single-molecule counts in each cluster. Using a Deming regression, data were fit to a linear function with a slope of 0.88 ± 0.15 for the RHL1 homo-oligomers and 0.45 ± 0.16 for the RHL1/RHL 2 hetero-oligomers.

1. Patterson GH, Lippincott-Schwartz J (2002) A photoactivatable GFP for selective photolabeling of proteins and cells. *Science* 297:1873–1877.
2. Subach FV, et al. (2009) Photoactivatable mCherry for high-resolution two-color fluorescence microscopy. *Nat Methods* 6:153–159.
3. Vámosi G, et al. (2008) Conformation of the c-Fos/c-Jun complex in vivo: A combined FRET, FCCS, and MD-modeling study. *Biophys J* 94:2859–2868.
4. Shroff H, et al. (2007) Dual-color superresolution imaging of genetically expressed probes within individual adhesion complexes. *Proc Natl Acad Sci USA* 104:20308–20313.
5. Betzig E, et al. (2006) Imaging intracellular fluorescent proteins at nanometer resolution. *Science* 313:1642–1645.
6. van Hulst NF, et al. (2000) Analysis of individual (macro)molecules and proteins using near-field optics. *J Chem Phys* 112:7799–7810.
7. Cheezum MK, Walker WF, Guilford WH (2001) Quantitative comparison of algorithms for tracking single fluorescent particles. *Biophys J* 81:2378–2388.
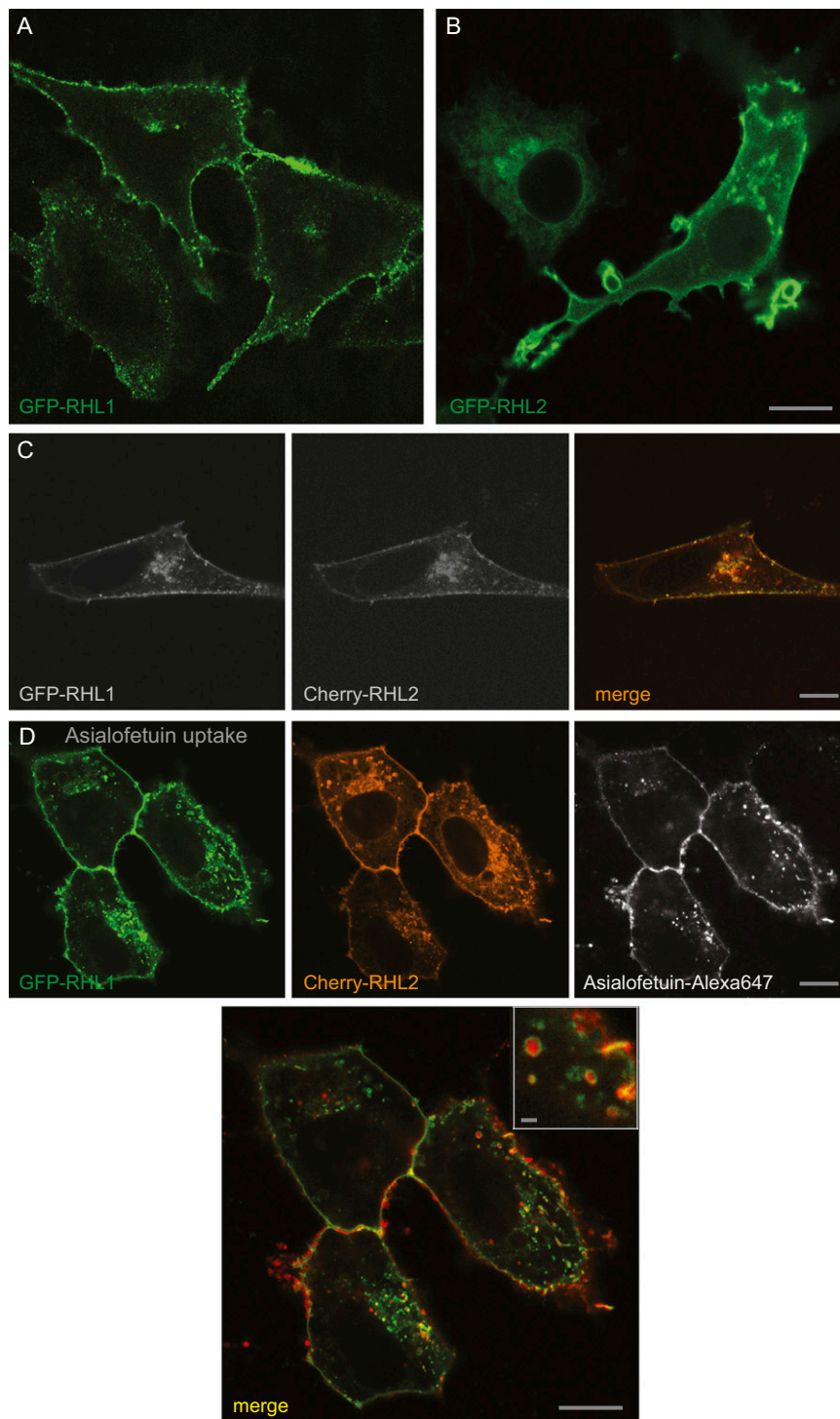
Fig. S1. Localization and functionality of fluorescent protein (FP) -labeled rat asialoglycoprotein receptor subunits expressed in live NRK cells. (*A*) GFP-RHL1 expressed in NRK cells showed a punctate distribution at the plasma membrane. It also localized to intracellular vesicles and perinuclear pools. (*B*) GFP-RHL2 expressed in NRK showed a homogenous distribution at the plasma membrane in contrast to GFP-RHL1. (*C*) Coexpressed with GFP-RHL1, Cherry-RHL2 adopted the punctate distribution of GFP-RHL1. (Scale bar: *A–C*, 10 μm.) (*D*) Functionality of the FP-labeled receptor subunits RHL1 and RHL2. Because RHL subunits had not been labeled with FPs yet, it was important to test the functionality of these receptor constructs. Coexpression of labeled RHL1 and RHL2 resulted in efficient Asialofetuin uptake. After ligand binding at 4 °C, NRK cells were incubated at 37 °C for 20 min and then fixed. Alexa647-labeled asialofetuin was visible in intracellular vesicles (magnified in *Inset*). (Scale bar: *D*, 10 μm; *D Inset*, 1 μm.)

A

```
RHL1    MTKDY-------------------QDFQHLDNENDHHQLQRGPPPAPRLL    31
        *  **+               +    *+  *      +       *  **+
RHL2    MEKDFQDIQQLDSEENDHQLIGDEEQGSHVQNLRTENPRWGGQPPSRPFP    50
```

                          transmembrane domain   stalk domain

```
RHL1    QRLCSGFRLFLLSLGLSILLLVVVCVITSQNSQLREDLRVLRQNFSNFTV    81
        *****  *** **+*   +*******+**+**+  **+++   *++   ***+
RHL2    QRLCSKFRLSLLALAFNILLLVVICVVSSQSMQLQKEFWTLKETLSNFST    100
```

```
RHL1    STEDQVKALTTQGERVGRKMKLVESQLEKHQEDLREDHSRLLLHVKQLVS    131
        +*   +  *** +  *         +     *+ ***  *+*++  ***  **  *+*
RHL2    TTLMEFKALDSHGGSRNDNLTSWETILEKKQKDIKADHSTLLFHLKHFPL    150
```

                                  C-type lectin domain

```
RHL1    DVRSLSCQMAALRGNGSERICCPINWVEYEGSCYWFSSSVKPWTEADKYC    181
        *+*+*+**+*    **+*  ***+****+ ******      *  ***+**
RHL2    DLRTLTCQLAFFLSNGTE--CCPVNWVEFGGSCYWFSRDGLTWAEADQYC    198
```

```
RHL1    QLENAHLVVVTSWEEQRFVQQHMGPLNTWIGLTDQNGPWKWVDGTDYETG    231
        *+*****+*+  *  *** **  +*  *    +  *******++* ********+*  +
RHL2    QMENAHLLVINSREEQEFVVKHRGAFHIWIGLTDKDGSWKWVDGTEYRSN    248
```

```
RHL1    FKNWRPGQPDDWYGHGLGGGEDCAHFTTDGHWNDDVCRRPYRWVCETELG    281
        ****    **+*+ **   ** ****     +** ***+  *++   ** **   +
RHL2    FKNWAFTQPDNWQGHEEGGSEDCAEILSDGLWNDNFCQQVNRWACERKRD    298
```

```
RHL1    KAN    284
RHL2    ITY    301
```

B
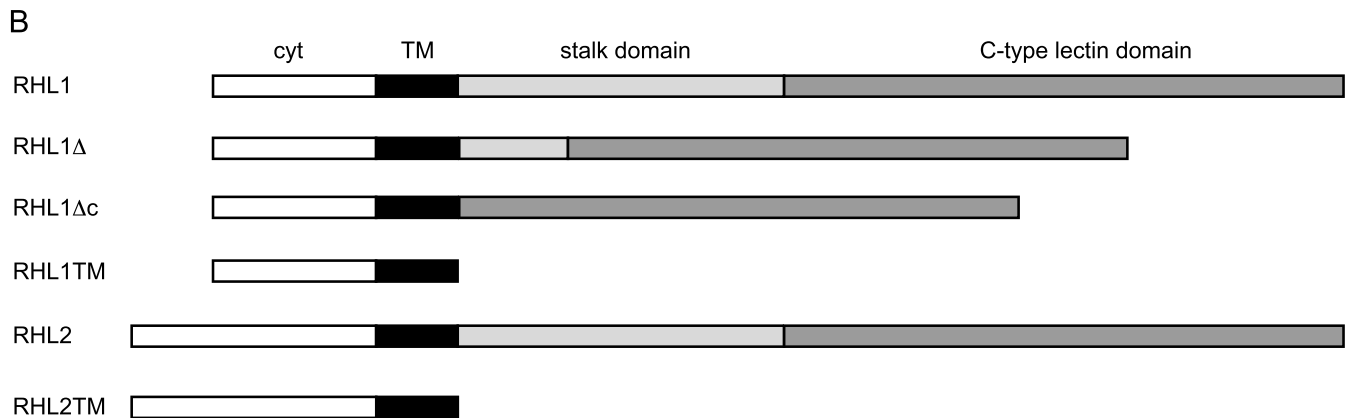
Fig. S2.   Sequence alignment of RHL1 and RHL2 and mutant RHL forms. (A) RHL1 and RHL2 are encoded by different genes; however, they share high sequence homology. Sequence alignment was performed by COBALT (National Center for Biotechnology Information). *, 46.1% of the amino acids are identical. +, 15.5% of the amino acids are homologous. (B) Scheme of mutant RHL forms analyzed in this study. In RHL1Δ (RHL1Δ68–119), two-thirds of the stalk domain are deleted. In RHL1Δc (RHL1Δ68–149), the entire stalk domain is deleted. Both mutants, RHL1TM (RHL1Δ67–284), and RHL2TM (RHL2Δ85–301), comprise only intracellular and transmembrane domains of RHL1 and RHL2, respectively.
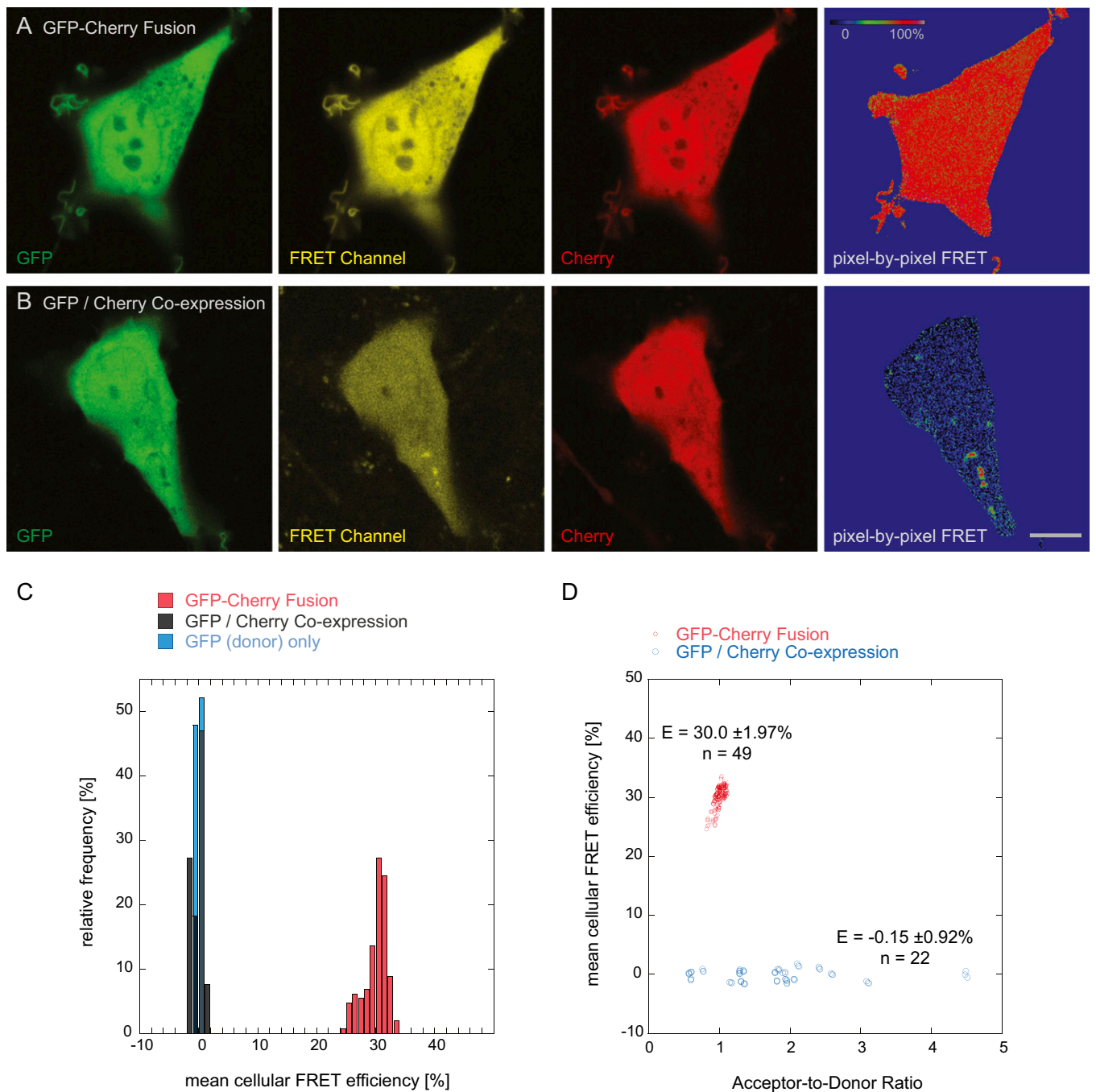
Fig. S3. FRET controls to determine sensitized emission by confocal microscopy. On each measurement day, cells expressing the GFP-Cherry fusion protein as positive control and coexpressing GFP and Cherry as negative control were analyzed to assess parameters of sensitized emission and the dynamic range of the FRET experiments. (*A*) Positive control: GFP-Cherry fusion protein expressed in NRK cells. (*B*) Negative control: GFP and Cherry coexpressed in NRK cells. (*C*) Distribution of cellular FRET efficiencies for positive control (GFP-Cherry fusion: 30.0 ± 1.9%, *n* = 49 cells) and negative controls (GFP/Cherry coexpression: −0.15 ± 0.92%, *n* = 22 cells; GFP only: 0.01 ± 0.03%, *n* = 23 cells). (*D*) Mean cellular FRET efficiencies of the positive and negative controls plotted vs. acceptor-to-donor ratio.
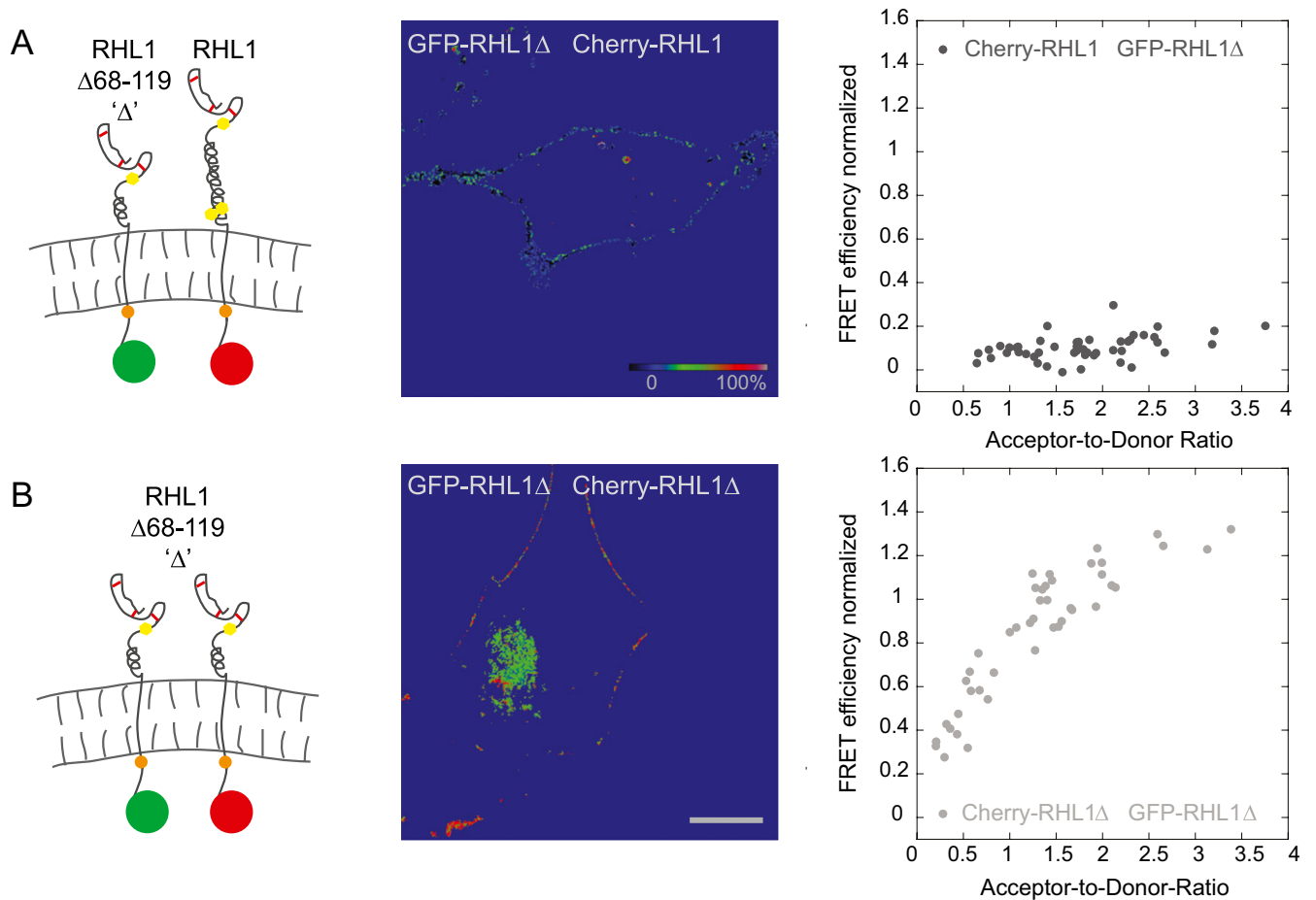
Fig. S4. Homo-oligomerization of RHL1 driven by its stalk domain. (*A*) Deletion of two-thirds of the stalk domain reduced the interaction between WT and mutant RHL1; normalized mean cellular FRET efficiencies were only about 5%. (*B*) FRET indicated a high tendency for self-association among the mutant RHL1 (RHL1Δ). The high tendency to homo-oligomerize of both WT and mutant RHL1 explained the low interaction between the two; avoiding populations of either RHL1 or RHL1Δ molecules formed tightly packed clusters. The cartoons depict the RHL1 or its mutant form, respectively. The images display color-coded FRET values in each pixel. The color-coded scale bar is for normalized mean FRET efficiencies. (Scale bar: *A* and *B*, 10 μm.) In the graphs, mean FRET efficiency integrated over the pixels showing the plasma membrane was plotted vs. the acceptor-to-donor ratio.
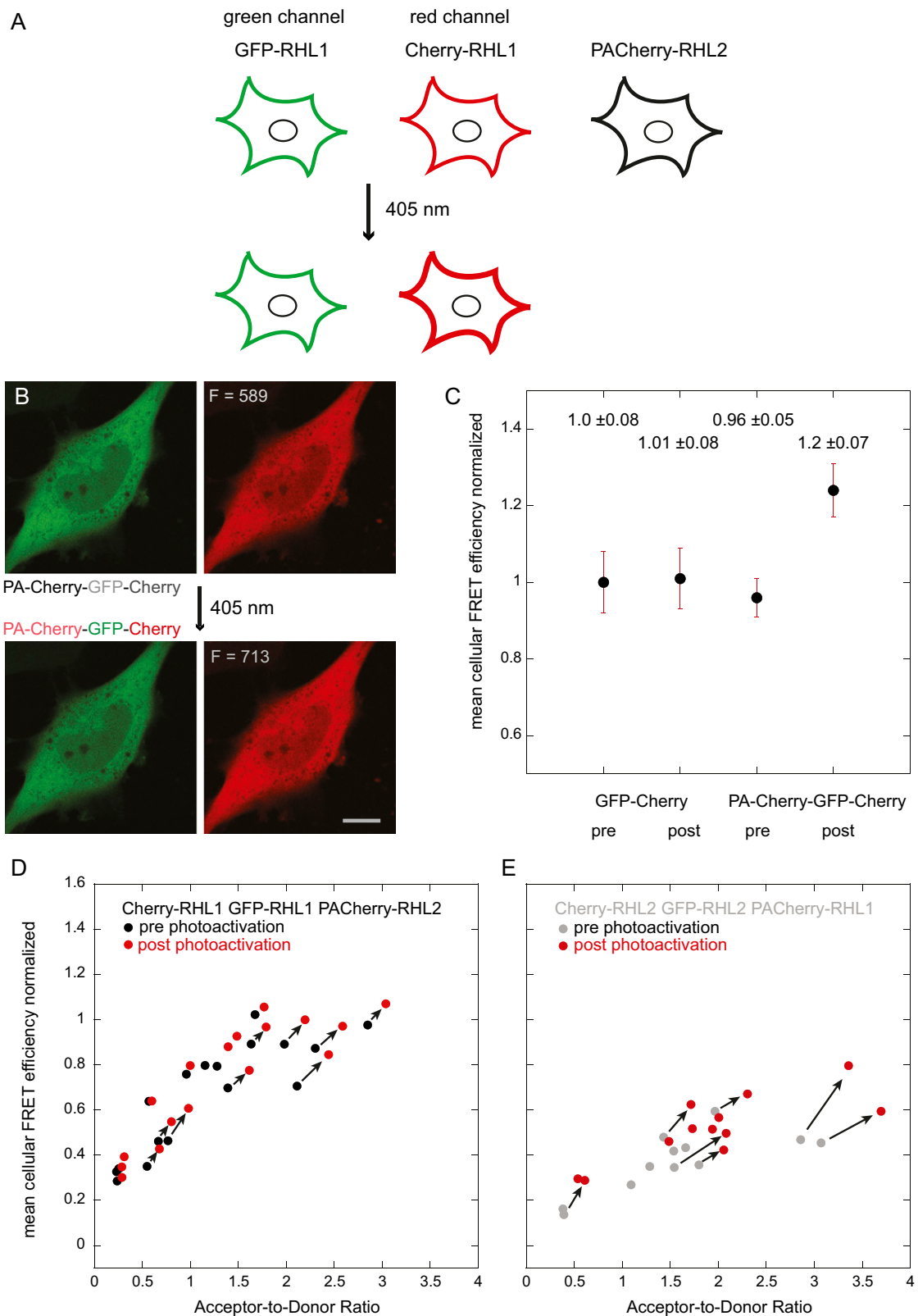
Fig. S5. Use of PA-Cherry as a transfection marker for ensemble FRET experiments. (*A*) FRET strategy for determining a change in homo-oligomerization of one subunit in the presence of the PA-Cherry–labeled other subunit. In cells coexpressing a GFP-RHL1, Cherry-RHL1, and PACherry-RHL2, the PA-Cherry construct should not affect FRET between the GFP-RHL1 and Cherry-RHL1 before photoactivation, unless the presence of RHL2 changes RHL1 self-association (Fig. 2*D*). Photoactivation of PA-Cherry-RHL2, however, should result in a significant increase in red fluorescence, and if RHL1 and RHL2 are forming hetero-oligmeric complexes, an increase in FRET efficiency after photoactivation should occur. Increase in red fluorescence and potentially FRET permit to reliably determine the presence of the PA-Cherry construct. We tested these requirements first using a cytoplasmic PACherry-GFP-Cherry triple fluorophore construct.

(*B* and *C*) NRK cell expressing the triple fluorophore construct PACherry-GFP-Cherry before and after photoactivation. Note the increase in red fluorescence F (from 589 a.u. before photoactivation to 713 a.u. after photoactivation). (Scale bar: *B* and *C*, 10 μm.) (*C*) Mean cellular FRET efficiencies measured before and after exposure to the same amount of 405-nm light. The measured FRET efficiency between GFP-Cherry remained unchanged, whereas the FRET efficiency between the triple construct, PA-Cherry-GFP-Cherry, increased significantly (from 0.96 ± 0.05 before to 1.2 ± 0.07 after photoactivation). (*D*) NRK cells expressing GFP-RHL1, Cherry-RHL1, and PA-Cherry-RHL2. Increase in mean cellular FRET efficiency and acceptor-to-donor ratio after photoactivation indicated the presence of PA-Cherry-RHL2 forming hetero-oligomeric complexes with RHL1. (*E*) NRK cells expressing GFP-RHL2, Cherry-RHL2, and PA-Cherry-RHL1. Increase in mean cellular FRET efficiency and acceptor-to-donor ratio after photoactivation indicated the presence of PA-Cherry-RHL1 forming hetero-oligomeric complexes with RHL2.
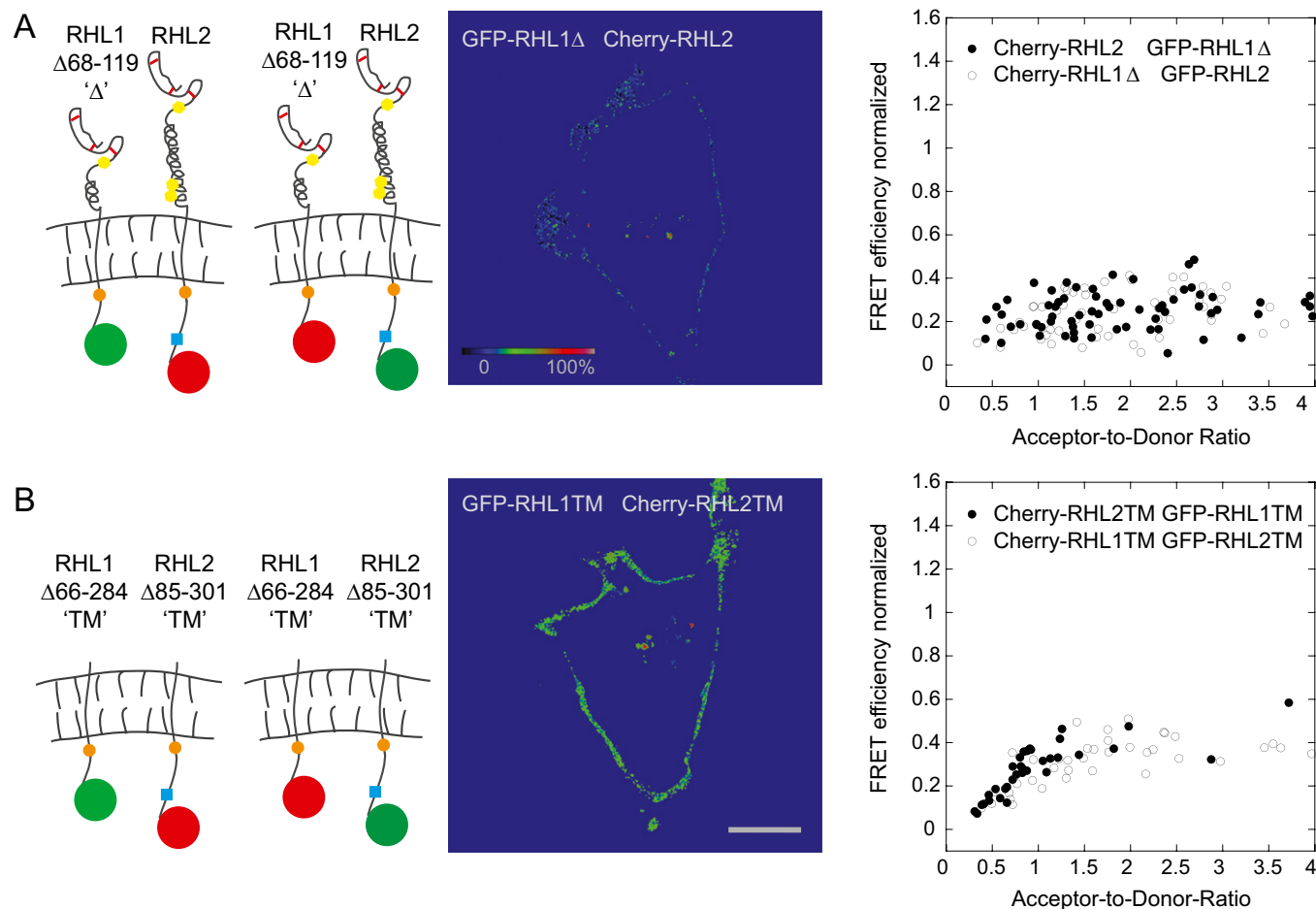
Fig. S6. Hetero-oligomerization of RHL1Δ, WT RHL2, and the transmembrane mutants RHL1TM and RHL2TM. (*A*) Deletion of two-thirds of the RHL1 stalk domain reduced the normalized mean cellular FRET between mutant RHL1 and WT RHL2 to about 20%. Please note the spread in detected FRET efficiencies. Apparently, various interactions are possible given a certain acceptor-to-donor ratio. Swapping colors did not result in a significant change in the detected FRET curve. (*B*) Basic interaction between RHL1 and RHL2 is mediated through transmembrane and intracellular domains. Deletion of all external domains resulted in a normalized FRET efficiency of about 35%. The cartoons depict the studied subunits or their mutant forms. The images display color-coded FRET values in each pixel. The color-coded scale bar is for normalized mean FRET efficiencies. (Scale bar: 10 μm.) In the graphs, mean FRET efficiency integrated over the pixels showing the plasma membrane was plotted vs. the acceptor-to-donor ratio.
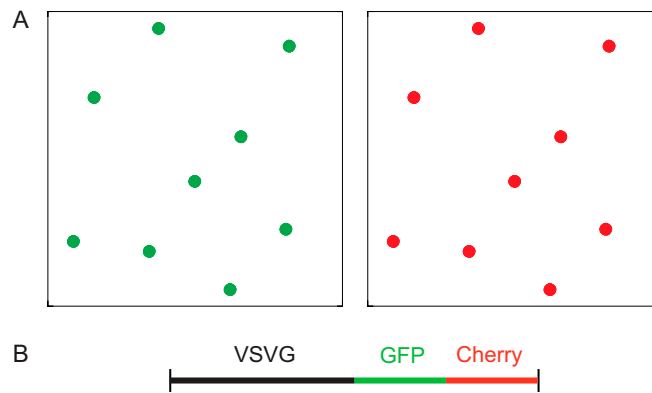
Fig. S7. Strategy for single-molecule counting PALM. Lightening up molecules one after the other, it is seemingly straightforward to obtain molecule numbers using PALM. However, it is critical to develop tools that permit validation of such assessed single-molecule counts. Because PALM works with genetically encoded FPs, the amount of proteins expressed varies from cell to cell and is unknown. Therefore, it has not been shown yet that PALM is capable of stably reproducing molecule numbers. A general way to validate counts is to count two times: for instance, molecules could be counted with PALM and then with another technique. Alternatively (the approach that we took in this study), molecules can be counted two times using PALM (for instance, first in green and then in red; see cartoon in *A*). Instead of tagging a fluorophore to an external reference, the fluorophore is tagged to a spectrally distinct second fluorophore. By coupling the genetic information of a green and a red PA-FP, internal rulers are created that will still be expressed to an unknown total amount but a fixed and known relative amount of 1:1. Measuring different cells expressing this construct, it can be tested if a specific ratio can be stably reproduced and thus, if single-molecule counting with PALM is possible. To minimize cytoplasmic pools and anchor molecules to the plasma membrane, the two irreversibly photoactivatable fluorescent proteins PA-GFP and PA-Cherry were tagged to the transmembrane protein VSVG (*B*). Based on the differential activatability of PA-GFP and PA-Cherry that we describe here, we developed an efficient sequential two-color PALM imaging regimen (Figs. S8 and S9). Then, we defined criteria to assign detected intensity peaks to single molecular events (Figs. S10 and S11). Ultimately, applying the imaging and analysis regimen to cells expressing the PA-GFP-PA-Cherry double construct, we were able to stably reproduce a specific red-to-green ratio in different cells expressing the test construct in different absolute amounts and thus, show that single-molecule counting with PALM is possible (Fig. 4*A*). In a cell-based dilution series, we showed that single-molecule counts scale linearly relative to each other and can be used to quantify the relative expression of red and green molecules in a given membrane area (Fig. 4*C*) or protein cluster (Fig. 4 *D* and *E*). Stoichiometries of two types of interacting proteins have been spectroscopically assessed using techniques based on intensities of at least a few molecules emitting simultaneously. Examples include variants of fluorescence correlation spectroscopy (FCS) (1), such as two-color photon-counting histogram (2), or two-color number and brightness approaches (3). However, these approaches require the assumption that a single molecule emits a certain amount of photons, and many molecules emit multiples of that. In contrast, PALM permits switching on molecules sequentially and irreversibly and therefore, enables the registration of discrete molecular events. As a single molecule-based imaging technique, PALM deals with absolute quantities rather than relative intensity values and therefore, permits a counting approach fundamentally different from intensity-based techniques. Having shown that single-molecule counting PALM is possible and can be used to assess the relative amount of spectrally distinct fluorescent proteins, it is probably critical to state that numbers of detected fluorescent molecules should not be simply taken as numbers of molecules expressed. Besides general challenges of single-molecule fluorescence studies (e.g., fluorophore maturation, sample preparation, sensitivity of the experimental setup, background, and thresholding), the PALM-specific feature of photoactivation needs to be taken into account.

1. Webb WW (2001) Fluorescence correlation spectroscopy: Genesis, evolution, maturation and prognosis. *Fluorescence Correlation Spectroscopy. Theory and Applications*, eds Rigler R, Elson EL (Springer, Berlin), pp 305–330.
2. Chen Y, et al. (2005) Dual-color photon-counting histogram. *Biophys J* 88:2177–2192.
3. Digman MA, Wiseman PW, Choi C, Horwitz AR, Gratton E (2009) Stoichiometry of molecular complexes at adhesions in living cells. *Proc Natl Acad Sci USA* 106:2170–2175.
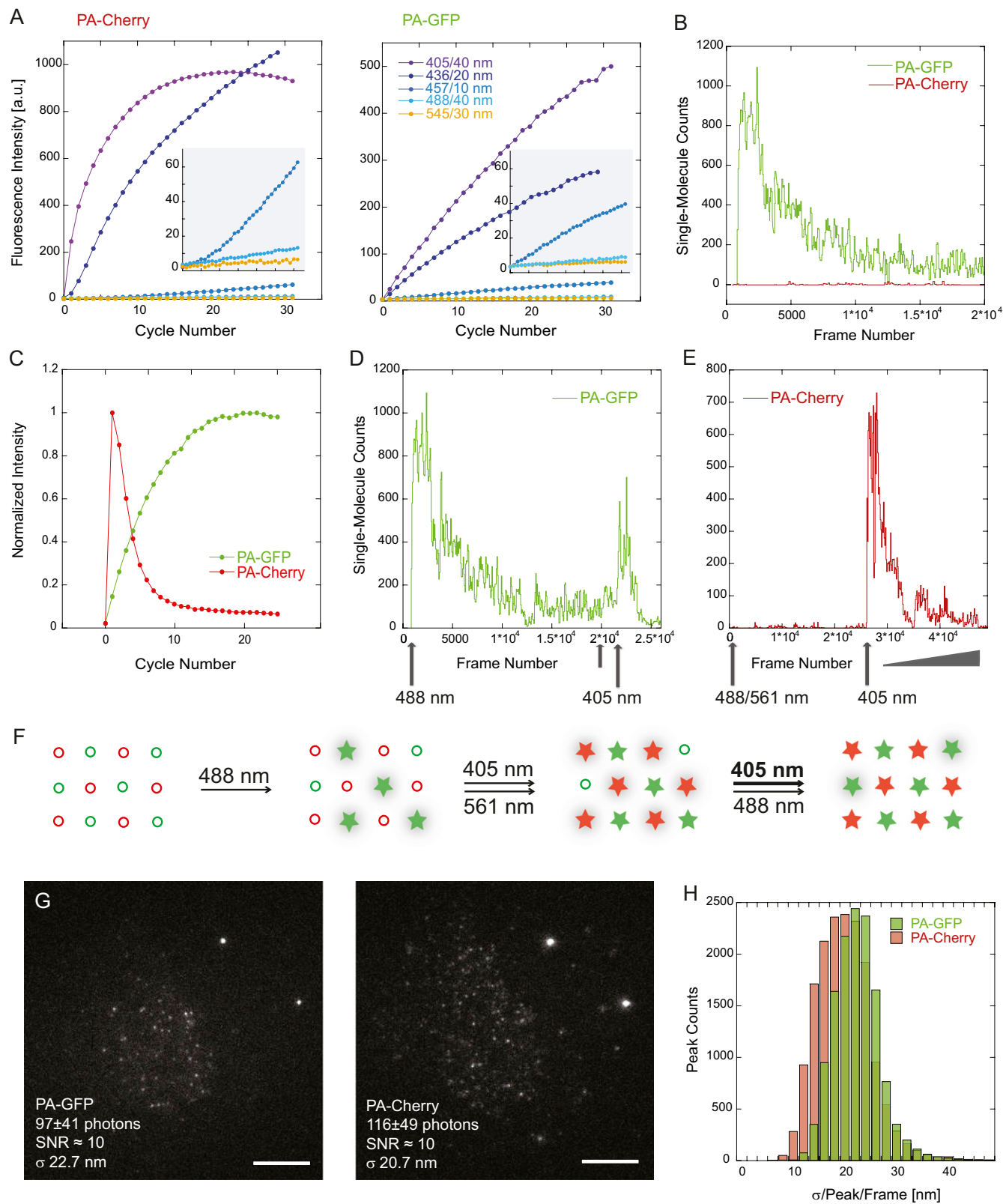
Fig. S8. Ensemble and single-molecule characterization of PA-GFP and PA-Cherry for sequential two-color PALM imaging. In ensemble and single-molecule studies, we were able to describe different fluorophores as differentially sensitive to UV light and activatable by light other than UV. The differential activatability set the basis for the protocol of efficient sequential two-color PALM imaging of PA-GFP and PA-Cherry. (*A*) Ensemble activation profiles of PA-GFP and PA-Cherry. To develop an efficient single-molecule detection regimen for counting PA-GFP and PA-Cherry in the same specimen, we explored the differential activatability of PA-GFP and PA-Cherry by different wavelengths of light. Previously, PA-GFP and PA-Cherry have been activated exclusively through UV light exposure (1). Using light of different wavelengths for ensemble activation revealed broad activation spectra for both PA-Cherry and PA-GFP. Mammalian cells were alternately exposed to 8 s of activating epifluorescence light and imaged with confocal laser scanning microscopy. For epifluorescence

activation, an arc lamp was used (90 μW for each band) along with one of the following band-pass filters: 405/40, 436/20, 457/10, 488/40, 545/30. (*Insets*) Magnification of activation profiles assessed by 457/10, 488/40, or 545/30. Note the rescaling of the *y* axis. (*B*) Single-molecule characterization of the differential activatability of PA-GFP and PA-Cherry by low 488-nm light (30 W/cm^2). Notably, single-molecule characterization showed that PA-GFP can efficiently be activated by low 488-nm light. When the same low 488-nm light was used to activate PA-Cherry, by contrast, virtually no signal is detected. (*C*) Ensemble study of the differential activatability of PA-GFP and PA-Cherry by low UV light. Cells were alternately exposed to 8 s of epifluorescence light (360/40) and imaged using confocal laser scanning microscopy. PA-Cherry reached its intensity maximum after one cycle of activation, whereas it took a longer time to activate fully PA-GFP. This finding indicated that PA-Cherry is more sensitive than PA-GFP to low-intensity UV light exposure and can be preferentially activated using low UV light. Fluorescence intensity was normalized to its maximum. A potential explanation for the differential activatability is that PA-GFP is in equilibrium between neutral phenolic and anionic phenolate states, with an absorbance peak at 397 nm and a minor peak at 475 nm. Ilumination with 488-nm light not only gradually depletes the anionic phenolate pool, acting as a sink for the larger neutral pool, but may also shift the equilibrium to its anionic state, which was reported for WT GFP (2). The sensitivity of PA-Cherry to low 405-nm light may be based on the fluorophore's property to store absorbed energy in a potential two-step mechanism of photoactivation. Note its sigmoidal activation profile in this context (*A*). (*D*) Single-molecule characterization of PA-GFP activation. PA-GFP was efficiently activated by the 488-nm light used (the first arrow indicates 488-nm activation and excitation alone set to low power density of 30 W/cm^2). The low 405-nm light used for PA-Cherry activation did not activate PA-GFP (the second arrow indicates the addition of low 405-nm light, which was used to activate PA-Cherry; i.e., 0.01–3 W/cm^2). Addition of higher power of 405-nm light, however, led to a second peak in single-molecule counts (the third arrow indicates the application of higher power of 405-nm light; i.e., 3 up to 500 W/cm^2). (*E*) Single-molecule characterization of PA-Cherry activation. PA-Cherry was not activated by 488-nm light (30 W/cm^2) but efficiently activated by low-dose UV light. The first arrow indicates illumination by 488- and 561-nm light, and the second arrow indicates the addition of 405-nm laser (405-nm laser intensity was increased from 0.01 to 3 W/cm^2). (*F*) Illumination scheme for sequential two-color PALM imaging using differential activatabilty of PA-GFP and PA-Cherry. The differential activatability of PA-GFP and PA-Cherry by different wavelengths and intensities of light enabled us to develop a sequential illumination regimen for optimal two-color imaging. First, low 488-nm light alone is used to activate and excite PA-GFP (30 W/cm^2). When no additional PA-GFP is registered, illumination is switched to 405-nm light to activate and low 561-nm light (40 W/cm^2) to excite PA-Cherry. Power density of the 405-nm laser is initially set to 0.01 W/cm^2 and gradually increased to 3 W/cm^2. After PA-Cherry is exhausted, 488-nm illumination is again applied, and 405-nm activation is set to high power density (3 up to 500 W/cm^2); 405-nm light is used to measure PA-GFP molecules, which might not have been accessible by 488-nm activation alone. (*G*) Representative frame of PA-GFP and PA-Cherry. Applying the described low-light illumination regimen to PA-GFP and PA-Cherry single-molecule imaging yielded low background for both colors. Achieved photon yield, signal-to-noise ratio (SNR), and precision (σ) of the 2D Gaussian fit per peak and frame are indicated. (Scale bar: 10 μm.) (*H*) Distribution of precision (σ) of 2D Gaussian fit per peak and frame. Note that PA-GFP rendered a just slightly higher uncertainty than PA-Cherry. These results contrast with the poor single-molecule imaging characteristics previously described for PA-GFP (1), which used 405-nm light for activation and 488-nm light for imaging. The high background noticed in these former studies could be caused by insufficiently bleached molecules rather than inactive molecules.

1. Shroff H, et al. (2007) Dual-color superresolution imaging of genetically expressed probes within individual adhesion complexes. *Proc Natl Acad Sci USA* 104:20308–20313.
2. Chattoraj M, King BA, Bublitz GU, Boxer SG (1996) Ultra-fast excited state dynamics in green fluorescent protein: Multiple states and proton transfer. *Proc Natl Acad Sci USA* 93: 8362–8367.
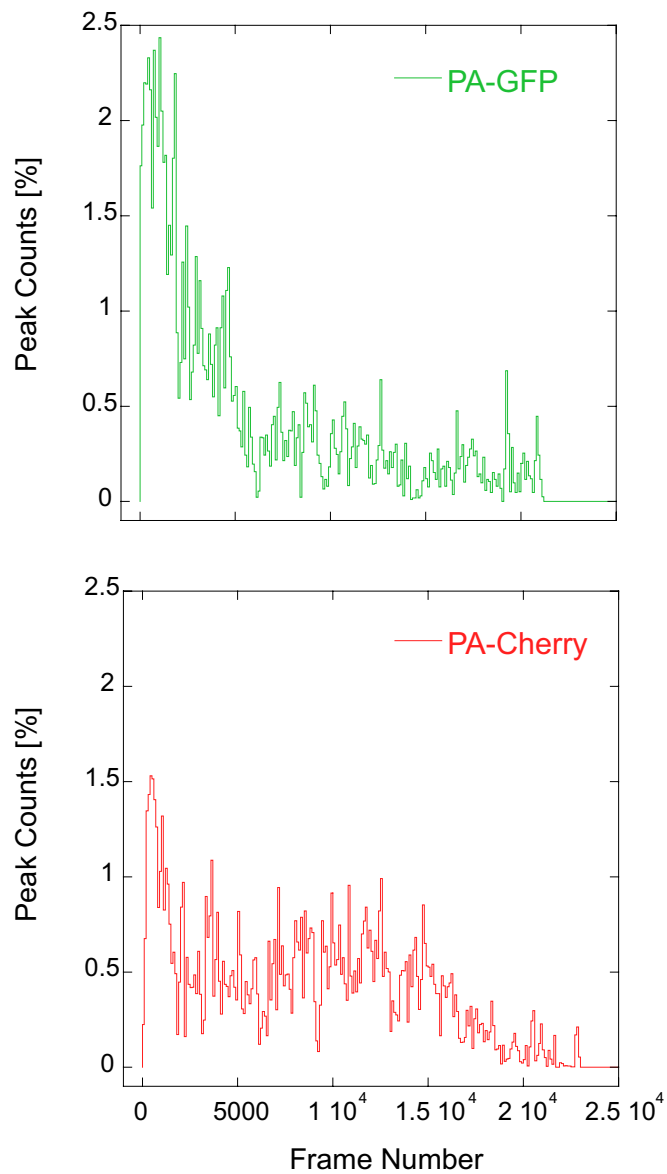
Fig. S9. Count rate traces of PA-GFP and PA-Cherry. Because PA-GFP was activated by 488-nm light set to a constant power density, whereas PA-Cherry was activated by gradually increasing 405-nm light, resulting count rate traces are different. It is critical not to crop measurements arbitrarily and in the case of PA-GFP, not to miss the initial count flare-up. Differential activatability and varying total fluorophore amount make the described illumination regimen for exhaustive single-molecule registration essential. Only then, a fixed relative amount can be stably reproduced.
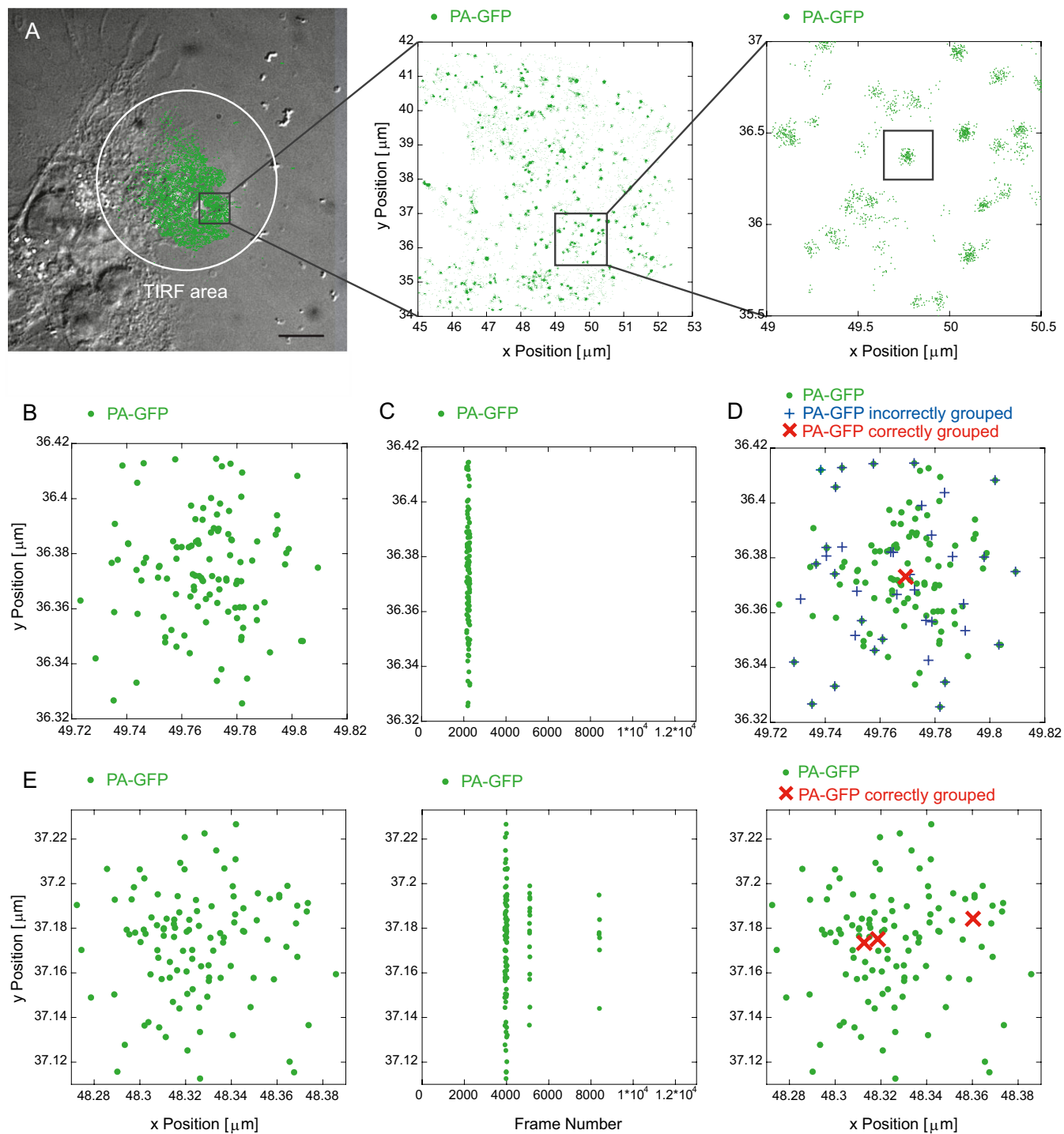
Fig. S10. Defining single molecular events. In PALM, a single fluorophore may emit photons over multiple consecutive frames before being photobleached. This result is especially true under conditions of low-light illumination because of less photobleaching. Is it possible then to avoid counting a single fluorophore as many when it is pictured in multiple consecutive frames? Because this is a prerequisite to assure correct single-molecule counts, we set out to determine a way to properly assign isolated intensity peaks to single molecules. COS-7 cells expressing VSVG-PA-GFP relatively sparsely (~10 molecules/μm^2) were imaged using the described illumination regimen. (*A*) Sequential zoom shows isolated peaks and their distribution. All intensity peaks from all frames collected during imaging are depicted in the TIRF area. When the black box in the TIRF area is enlarged, clouds of PA-GFP intensity peaks of differing sizes can be seen that are widely dispersed. Zooming in on a smaller area reveals that each cloud of PA-GFP is comprised of a discrete cluster of intensity peaks. (Scale bar: 10 μm.) (*B*) Magnifying one of these clusters shows a specific distribution of individual peaks, with peaks most concentrated in the central area. (*C*) Plotting y position against frame number of this exemplarily chosen mini cluster. All peaks appeared in a narrow window of time (i.e., frames 2,130–2,300). Because there were no other intensity peaks generated in this area over the entire imaging period, the simplest interpretation is that the cluster of peaks represents one and the same molecule pictured over multiple frames. Its distribution can be explained with the uncertainty associated with peak fitting in each frame. (*D*) Different grouping regimens result in diverse single-molecule counts and spatial organization. We used the intensity peak distributions of single molecules sparsely expressed in a mammalian cell as the basis for adapting the grouping parameters. Grouping parameters define spatial and temporal limits within which isolated peaks are assumed to originate from one molecule. While the spatial limit is based on the fit precision, the temporal limit considers how long a fluorescent protein can blink off. Blinking

characteristics of fluorescent proteins in the long-time range are poorly characterized. GFP off-times may last up to several seconds (1). We found that using a grouping radius of 67 nm and a blinking time of 4 s permitted the collapse of clusters of intensity peaks into a single molecular event (red ×). By contrast, using a smaller grouping radius (i.e., 25 nm) and shorter blinking time (i.e., 1 s) led to peak clusters being erroneously assigned to many different molecules (blue crosses). Fig. S11 further illustrates this finding. Correct grouping: blinking time = 4 s; grouping radius = 67 nm. Incorrect grouping: blinking time = 1 s; grouping radius = 25 nm. (*E*) With the determined grouping parameters, it was possible to resolve in time the shown cluster of isolated intensity peaks as arising from three different molecules.

1. van Hulst NF, et al. (2000) Analysis of individual (macro)molecules and proteins using near-field optics. *J Chem Phys* 112:7799–7810.
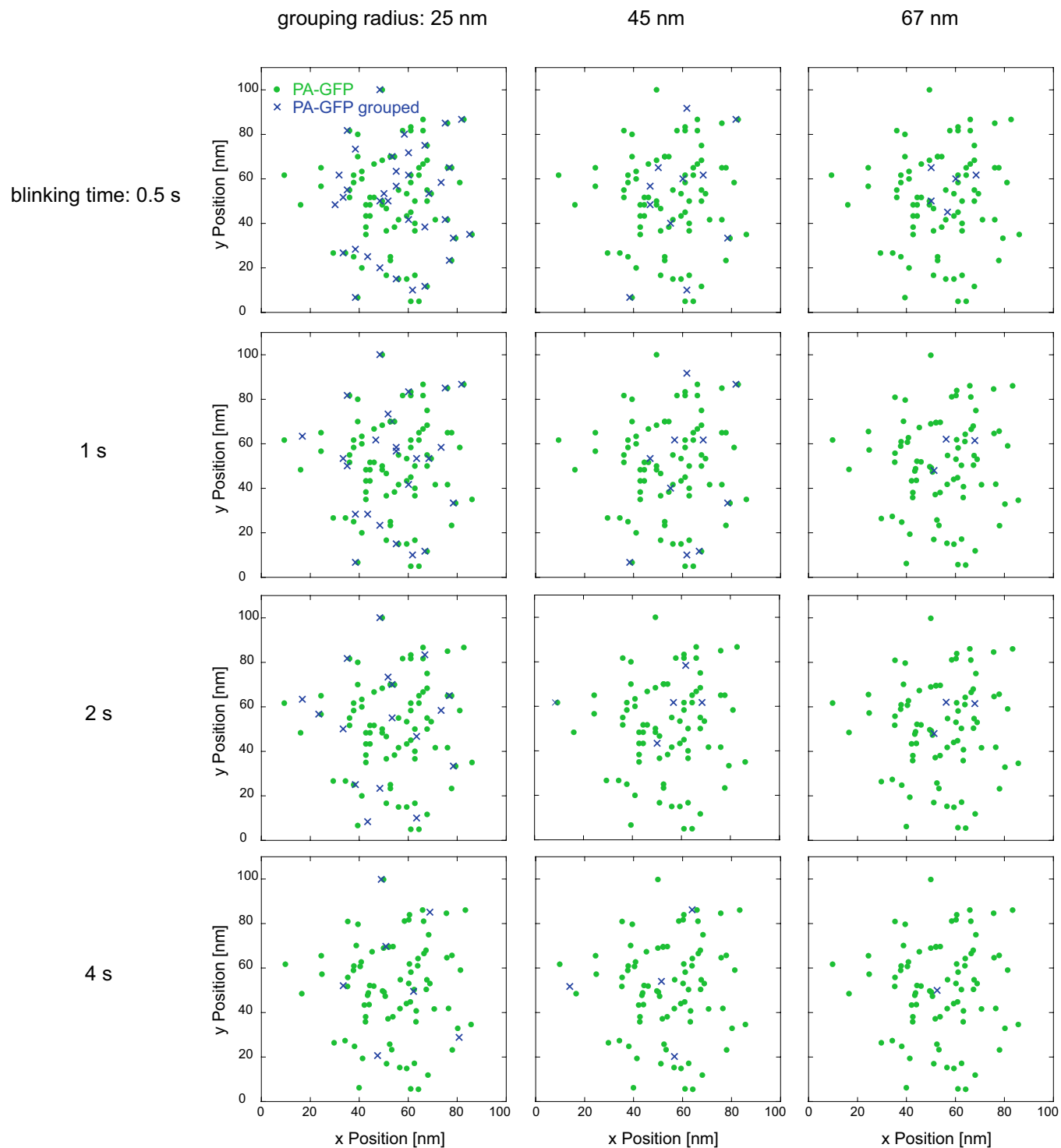
Fig. S11. Assigning isolated intensity peaks to single molecules considering different grouping radii and blinking times. The described illustrative approach permits assignment of isolated peaks to single molecules for any experimental setup. This approach is important, because sample preparation, illumination power and frequency, and intra- or extracellular labeling are likely to influence photostability and blinking characteristics of PA-FPs. The quality of the experimental setup determines fit precision and thereby the grouping radius.
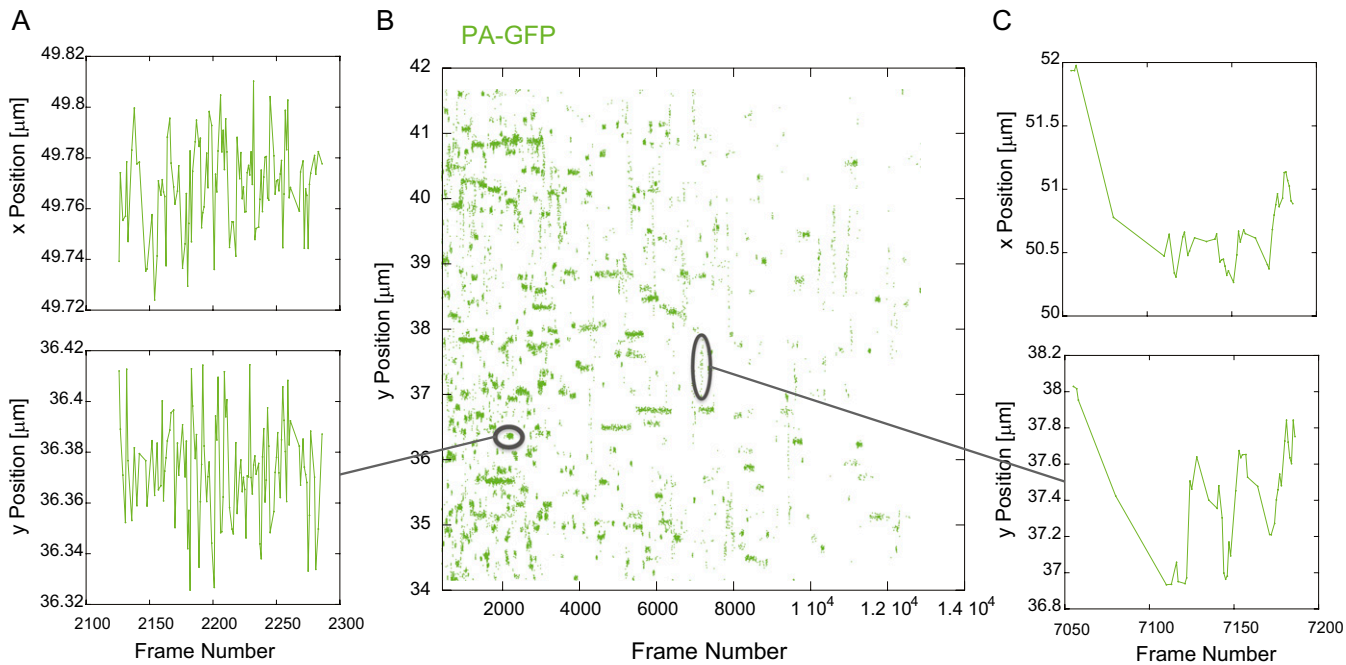
Fig. S12. Identification of properly fixed and still mobile molecules. Plotting a larger *y* range against frame number, reveals a population of insufficiently fixed, still mobile molecules. Those molecules cover a large distance (up to 1 μm) in a short time. (*A*) Zoom-in example of a properly fixed molecule; *x* and *y* positions are plotted against frame number. The corresponding raw data are in Movie S2. (*B*) Plotting *y* position against frame number. (*C*) Zoom-in example of an insufficiently fixed, still mobile molecule; *x* and *y* positions are plotted against frame number. The corresponding raw data are in Movie S3.

Movie S1. Image quality achieved by using 488-nm light alone to activate and excite PA-GFP. To not lose molecules at the beginning of any data acquisition, acquisition was started while searching for transfected cells.
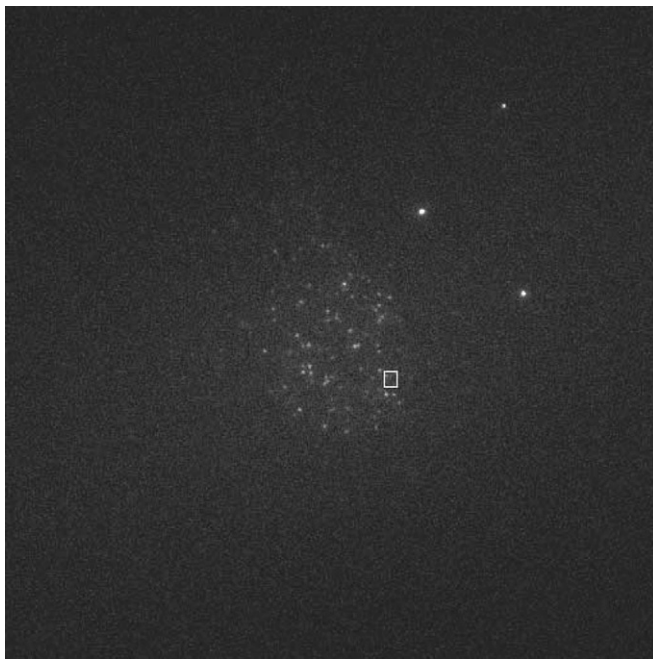
Movie S1

Movie S2. PA-GFP blinking. Example in a sparsely expressing cell outlined by the white frame. Corresponding isolated peaks are shown in Fig. S12*A*.

Movie S2
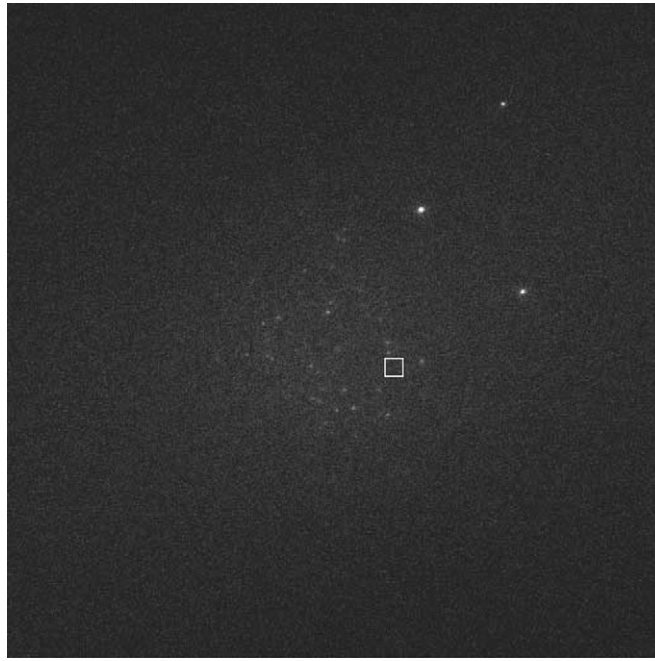
Movie S3.   Visualization of an insufficiently fixed, still mobile PA-GFP molecule outlined by the white frame. Corresponding isolated peaks are shown in Fig. S12C.

Movie S3